Journal of Solid State Chemistry 184 (2011) 2250–2256

Contents lists available at ScienceDirect

Journal of Solid State Chemistry

journal homepage: www.elsevier.com/locate/jssc

Insights into photoluminescence property and photocatalytic activity of cubic and rhombohedral $ZnIn_2S_4$

Shaohua Shen*, Penghui Guo, Liang Zhao, Yuanchang Du, Liejin Guo*

State Key Laboratory of Multiphase Flow in Power Engineering, Xi'an Jiaotong University, Shaanxi 710049, China

ARTICLE INFO

Article history:
Received 29 April 2011
Received in revised form
22 June 2011
Accepted 26 June 2011
Available online 1 July 2011

Keywords:
$ZnIn_2S_4$
Photocatalytic H_2 evolution
Photoluminescence property
Crystal phase

ABSTRACT

Cubic and rhombohedral $ZnIn_2S_4$ were synthesized by thermal sulfidation of Zn–In mixed oxide precursor in H_2S atmosphere at different temperatures. Cubic $ZnIn_2S_4$ was obtained when Zn–In mixed oxide precursor was sulfurized at 400 °C. With sulfidation temperature increasing from 400 to 800 °C, the crystal phase of $ZnIn_2S_4$ gradually turned from cubic to rhombohedral, which was demonstrated by different analysis techniques such as XRD, Raman, SEM, etc. UV–vis absorption spectra indicated that cubic $ZnIn_2S_4$ displayed better light absorption property than rhombohedral $ZnIn_2S_4$, with band gaps calculated to be 2.0 and 2.5 eV, respectively. However, under visible light irradiation, rhombohedral $ZnIn_2S_4$ photocatalyzed H_2 evolution from aqueous sodium sulfite/sulfide solution efficiently, whereas cubic $ZnIn_2S_4$ was not active for this reaction. The photoluminescence property revealed the different dynamics of photogenerated carriers, which made a predominant contribution to the increasing photocatalytic performances of $ZnIn_2S_4$ with crystal phase turning from cubic to rhombohedral.

1. Introduction

Photocatalytic water splitting has attracted intense attention and emerged as a viable option of solar to hydrogen conversion, since TiO_2 was used by Fujishima and Honda [1] acting as a photoanode to split water into H_2 and O_2 in a photoelectrochemical cell. In the few past decades, many wide band gap semiconductors have been developed to be active for photocatalytic water splitting and some of them achieved high quantum yields under ultraviolet light (UV) irradiation [2]. Nevertheless, in order to efficiently utilize solar energy, semiconducting photocatalysts which were active for H_2 production under visible light irradiation must be developed. Therefore, many efforts have been focused on the development of visible-light-driven photocatalysts [2], and some of which had high photocatalytic activities for H_2 production under visible light irradiation, when an S^{2-}/SO_3^{2-} solution was used as the electron donor [2]. Especially, Pt–PdS/CdS was recently reported to display an extremely high quantum yield reaching 93% at 420 nm, which was quite close to the energy efficiency level of natural photosynthesis with quantum yield as high as 95% [3].

On the other hand, because of the hypertoxicity of Cd^{2+} in CdS, some novel multicomponent metal sulfide systems, including Zn(Cu)–In–S [4–10], Ag(Cu)–Ga(In)–S [11–14], Cu–Ge(Zn)–S [15,16], Na–In(Cu)–S [17,18], Zn–In–Cu(Ag)–S [19–25], etc., have been explored to work as nontoxic photocatalysts for efficient H_2 production from the S^{2-}/SO_3^{2-} solution under visible light irradiation. In our previous studies [5,6,26,27], hydrothermally synthesized hexagonal $ZnIn_2S_4$ with layered structure (Fig. 1(A)) as a visible-light-active photocatalyst has been systematically investigated. The photocatalytic activity for H_2 evolution over hexagonal $ZnIn_2S_4$ could be greatly improved by crystal structure distortion along *c*-axis [26] as well as Cu^{2+} doping [6]. Till now, cubic and hexagonal $ZnIn_2S_4$, as depicted in Fig. 1(B) and (C), respectively, have been successfully synthesized by different methods, and showed a good photocatalytic activity under visible light [4,28–32]. However, there are very few reports that $ZnIn_2S_4$ of rhombohedral phase, as depicted in Fig. 1(C), worked as photocatalysts for H_2 evolution under visible light irradiation. In recent years, thermal sulfidation has been demonstrated to be one of the most effective methods to synthesize metal sulfides with good crystallinity and photocatalytic activities. For example, CdS [33] and $Cd_xZn_{1-x}S$ [34] obtained by thermal sulfidation of oxide precursor in H_2S atmosphere achieved high quantum yields of 24.1% and 10.2% at 420 nm for photocatalytic H_2 evolution, with 3 wt% Pt loading and even without any noble metal as cocatalysts, respectively.

In the present study, cubic and rhombohedral $ZnIn_2S_4$ were synthesized by thermal sulfidation of Zn–In mixed oxide precursor in H_2S atmosphere at different temperatures. The effects of sulfidation temperature on morphology, crystal structure, optical properties and photocatalytic activities of these $ZnIn_2S_4$ samples were investigated in detail. Moreover, it is interesting to note that the photoluminescence

* Corresponding authors. Fax: +86 29 82669033.
E-mail addresses: shshen_xjtu@mail.xjtu.edu.cn (S. Shen), lj-guo@mail.xjtu.edu.cn (L. Guo).

0022-4596/$ - see front matter © 2011 Elsevier Inc. All rights reserved.
doi:10.1016/j.jssc.2011.06.033

property revealed the different dynamics of photogenerated carriers, which played an important role in the photocatalytic performances of $ZnIn_2S_4$ with different crystal structures.

2. Experimental section

2.1. Synthesis of $ZnIn_2S_4$ samples

All chemicals are of analytical grade and used as received without further purification. $ZnIn_2S_4$ was prepared by thermal sulfidation of the oxide precursor. In a typical procedure, the stoichiometric amount of $Zn(NO_3)_2 \cdot 6H_2O$ (0.5955 g) and $In(NO_3)_3 \cdot 4.5H_2O$ (1.5277 g) was dissolved in a small amount of distilled water. The solution was evaporated to dryness on the hot plate under stirring; the resulting solid was heated in a quartz tube at 500 °C for 2 h in flowing air to obtain Zn–In oxide precursor. Dry H_2S (20–30 mL/min) gas was then passed through the quartz tube at 300–800 °C for 4 h to sulfurize oxide precursor into $ZnIn_2S_4$. After being cooled naturally to room temperature with flowing H_2S gas, orange or yellow colored powders were obtained and labeled as $ZnIn_2S_4$-T (T=300, 400, 500, 600, 700, and 800), here T represents the temperature (300–800 °C) at which the oxide precursor was treated with H_2S gas.

2.2. Characterization

The X-ray diffraction (XRD) patterns were obtained from a PANalytical X'pert MPD Pro diffractometer using Ni-filtered Cu $K\alpha$ irradiation (Wavelength 1.5406 Å). A Raman scattering study was performed on a Jobin Yvon LabRAM HR spectrometer using 514.5 nm irradiation from an argon ion laser at 20 mW. The sample morphology was observed by a JEOL JSM-6700FE scanning electron microscope. The diffuse reflection of the samples was determined by a Hitachi U-4100 UV–vis-near-IR spectrophotometer. The analysis of photoluminescence spectra (PL) was carried out at room temperature using a PTI QM-4 photoluminescence spectrophotometer.

2.3. Evaluation of photocatalytic activity

Photocatalytic hydrogen evolution was performed in a gas-closed circulation system with a top window Pyrex cell. A 300 W Xe lamp was used as the light source, and the UV part of the light was removed by a cutoff filter ($\lambda > 430$ nm). Hydrogen evolved was analyzed by an online thermal conductivity detector (TCD) gas chromatograph (NaX zeolite column, nitrogen as a carrier gas) every 10 min. In all experiments, the photocatalyst powder (0.2 g) was dispersed by a magnetic stirrer in 150 mL of 0.25 M Na_2SO_3/0.35 M Na_2S aqueous solution. Here, Na_2SO_3/Na_2S mixed sacrificial agent was used to scavenge photogenerated holes. Nitrogen was purged through the cell before reaction to remove oxygen. Pt (1 wt%) as a cocatalyst for the promotion of hydrogen evolution was photodeposited in situ on the photocatalysts from the precursor of $H_2PtCl_6 \cdot 6H_2O$. The temperature for all the photocatalytic reactions was kept at 25 ± 0.5 °C. The control experiments showed no appreciable H_2 evolution in the absence of irradiation or photocatalyst.

3. Results and discussion

3.1. Crystal structure

Fig. 2 shows the XRD patterns of $ZnIn_2S_4$ samples ($ZnIn_2S_4$-T, T=300–800) synthesized in H_2S atmosphere at different temperatures. When the $ZnIn_2S_4$ sample was obtained by sulfurizing oxide precursor at 300 °C, only the diffraction pattern from the

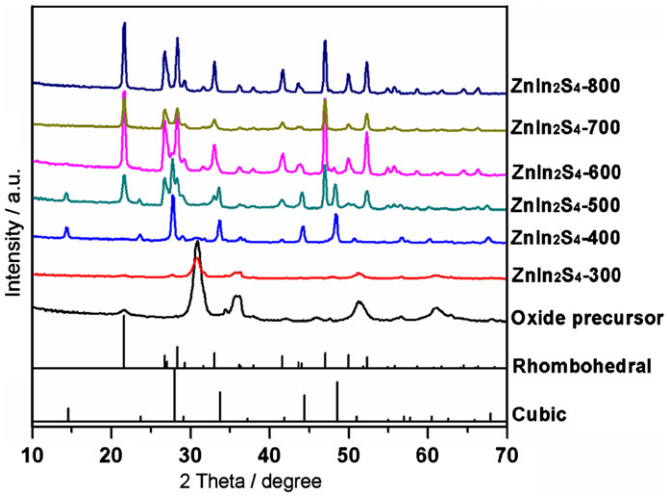

Fig. 2. XRD patterns of $ZnIn_2S_4$ synthesized in H_2S atmosphere at different temperatures.

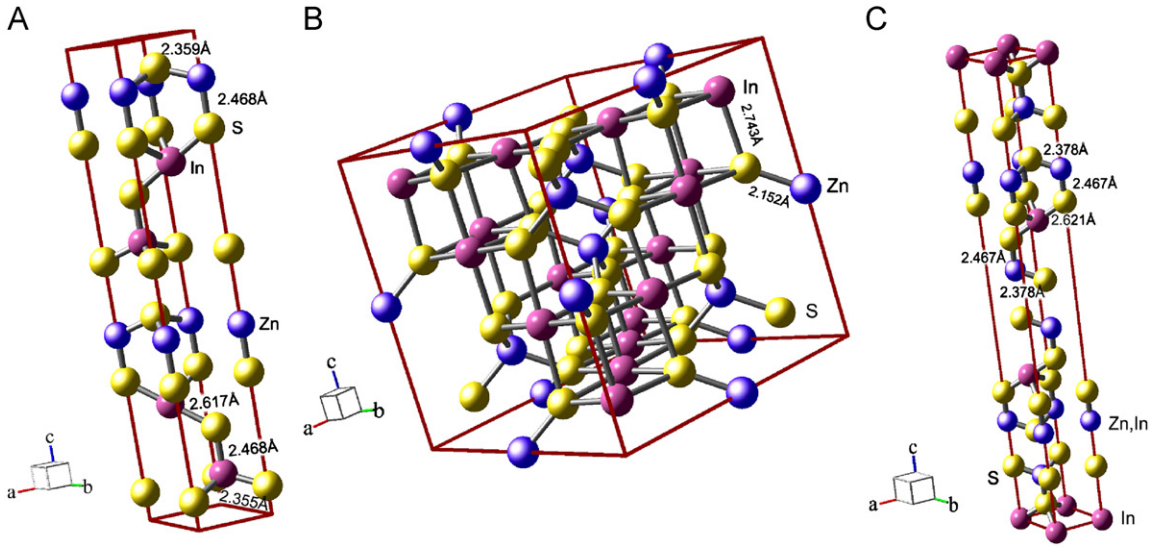

Fig. 1. Crystal structures of (A) hexagonal, (B) cubic and (C) rhombohedral $ZnIn_2S_4$.

Zn–In oxide precursor was observed, indicating that this temperature was not high enough to sulfurize oxide precursor to $ZnIn_2S_4$. Increasing the sulfidation temperature to 400 °C resulted in the formation of cubic $ZnIn_2S_4$ as identified by the signature cubic $ZnIn_2S_4$ reflection (ICSD-JCPDS card no. 00-048-1778, $a=10.62$ Å). When the sulfidation temperature was raised to 500 °C, rhombohedral $ZnIn_2S_4$ (ICSD-JCPDS card no. 00-049-1562, $a=3.86$ Å, $c=37.01$ Å) crystallites began to form, co-existing with cubic $ZnIn_2S_4$ phase. With the sulfidation temperature rising from 500 to 700 °C, the intensity of diffraction peaks assigned to cubic phase decreased, while the ones assigned to rhombohedral phase increased significantly. Rhombohedral $ZnIn_2S_4$ was the only crystalline phase observed when the oxide precursor was sulfurized at 800 °C.

Fig. 3 shows the Raman spectra of $ZnIn_2S_4$ samples ($ZnIn_2S_4$-T, $T=300$–800) synthesized in H_2S atmosphere at temperatures from 300 to 800 °C. The sample obtained by sulfidation at 300 °C did not display any characteristic band of Raman shift attributed to $ZnIn_2S_4$. Thus, the $ZnIn_2S_4$-300 sample still kept at the state of Zn–In mixed oxide. The absence of the bands assigned to the oxide precursor is likely due to a low signal-to-noise ratio for this sample. For the $ZnIn_2S_4$-400 sample obtained by sulfidation at 400 °C, three respective bands of Raman shift were observed at around 241, 301, and 350 cm^{-1}, which should be assigned to the longitudinal optical mode (LO_1), transverse optical mode (TO_2) and second-harmonic longitudinal optical mode (LO_2), respectively, resulting from the long-wavelength lattice vibrations of $ZnIn_2S_4$ [35,36]. Moreover, when elevating the temperature from 400 to 800 °C, the fourth band at 334 cm^{-1} in the Raman spectra of $ZnIn_2S_4$-400 became weaker and weaker, whilst the band at 362 cm^{-1} appeared gradually and became visible in the Raman spectra of $ZnIn_2S_4$-800. Obviously, this change was regular with the change of crystal structure from cubic to rhombohedral phase suggested by XRD data. Thus, these two bands at 334 and 362 cm^{-1} could be related to the Raman shift of cubic and rhombohedral $ZnIn_2S_4$, respectively, even though the supporting information about their attribution from previous references was limited [37].

The crystal structure changes associated with sulfidation temperature can be understood fully by examining the XRD patterns and Raman spectroscopy data discussed above. As the $ZnIn_2S_4$-300 sample still presented in the form of oxide precursor as indicated by XRD and Raman analysis, in the following section our discussion will focus on the morphology, optical and photocatalytic properties of the $ZnIn_2S_4$ samples obtained by sulfidation at different temperatures from 400 to 800 °C, $ZnIn_2S_4$-T ($T=400$–800).

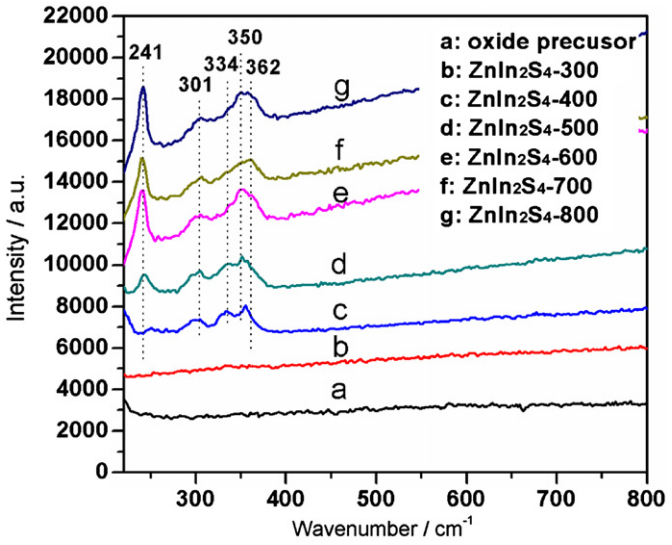

Fig. 3. Raman spectra of $ZnIn_2S_4$ synthesized in H_2S atmosphere at different temperatures.

3.2. Morphology

Fig. 4 shows the SEM images of oxide precursor and $ZnIn_2S_4$ samples ($ZnIn_2S_4$-T, $T=400$–800) synthesized in H_2S atmosphere at different temperatures from 400 to 800 °C. The oxide precursor (Fig. 4A) mainly existed as irregular lumps in micron-scale size. Well-crystallized particles with particle sizes of 100–200 nm were observed for $ZnIn_2S_4$-400 as shown in Fig. 4B. As observed from Fig. 4B to F, the gradually changed morphology of these $ZnIn_2S_4$ samples also hinted the crystal structure changing from cubic to rhombohedral phase as the sulfidation temperature increased from 400 to 800 °C.

3.3. Optical properties

Fig. 5 shows the UV–vis absorption spectra of $ZnIn_2S_4$ samples ($ZnIn_2S_4$-T, $T=400$–800) synthesized in H_2S atmosphere at different temperatures from 400 to 800 °C. The $ZnIn_2S_4$-400 sample with cubic structure exhibited good absorption property in visible light region; the absorption onset was observed at ca. 610 nm and absorbance became larger with a decrease in the wavelength. The absorption onsets of the $ZnIn_2S_4$-T ($T=400$–800) samples were blue-shifted from ca. 610 to 520 consistently with the gradual change of crystal structure from cubic to rhombohedral phase, induced by sulfidation temperature rising from 400 to 800 °C. Moreover, the shape of their absorption bands with steep edges in the visible-light region indicated that the visible-light absorption was due to a band transition, not due to the transition from impurity levels to the conduction band as observed for some ion-doped photocatalysts [38–40]. It has been reported that cubic and rhombohedral $ZnIn_2S_4$ are indirect-allowed [28] and direct-allowed semiconductors [41], respectively. Thus, as shown in Fig. 5(B and C) the corresponding band gaps of cubic and rhombohedral $ZnIn_2S_4$ were determined to be 2.0 and 2.5 eV, respectively, according to the Kubelka–Munk equation.

Photoluminescence spectra have been used widely to examine the efficiency of charge transfer, migration, separation and to understand the lifetime of photogenerated charges in semiconductors. The $ZnIn_2S_4$ samples ($ZnIn_2S_4$-T, $T=400$–800) showed photoluminescence at room temperature as shown in Fig. 6. For the $ZnIn_2S_4$-400 sample with cubic structure, the emission peak centered at 600 nm was very weak, possibly due to a large density of lattice defects induced non-radiative centers reducing the emission intensity. Such non-radiation transition was reported to be dominant in indirect semiconductors [42], leading to the weak emission intensity. When shifting focus on the $ZnIn_2S_4$-T ($T=500$–800) samples, the excitation peak around 425 nm was found to be caused by the band-to-band transition [41]. We could also observe that the onsets of excitation spectra monitored at 690 nm were in the position close to those of UV–Vis absorption spectra, which indicated that the emission centered at 690 nm of the $ZnIn_2S_4$-T ($T=500$–800) samples was derived from band gap excitation [43]. This emission band is in good agreement with the previous results [44]. Moreover, the emission intensity of the $ZnIn_2S_4$-T ($T=400$–800) samples gradually increased as the sulfidation temperature increased from 400 to 800 °C, with crystal structure changed from cubic to rhombohedral, and arrived at the highest degree for $ZnIn_2S_4$-800 with single phase of rhombohedral. Consequently, the photoluminescence measurements indicated that the efficiency of the non-radiative transition in $ZnIn_2S_4$-800 with rhombohedral structure was least, whereas it was dominant in cubic $ZnIn_2S_4$, i.e., $ZnIn_2S_4$-400. The non-radiative transition was reported to not only affect the photoluminescence but also the photocatalytic activity [45], as non-radiative transition always led to photoluminescence

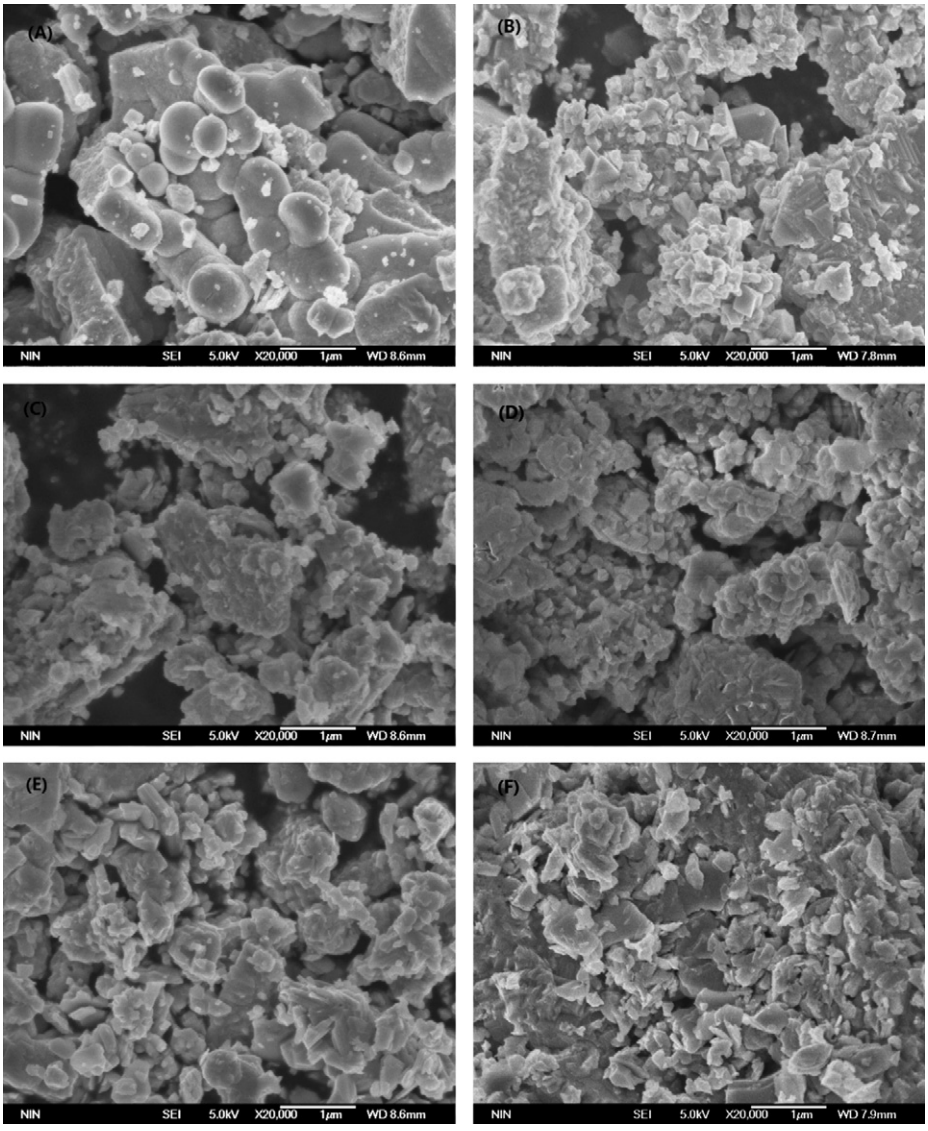

Fig. 4. SEM images of $ZnIn_2S_4$ synthesized in H_2S atmosphere at different temperatures, (A) oxide precursor, (B) 400 °C, (C) 500 °C, (D) 600 °C, (E) 700 °C and (F) 800 °C.

quenching, which meant decreased number of electrons and holes available for photocatalytic reaction. The relationship between the photocatalytic activity and emission intensity of the $ZnIn_2S_4$-T (T=400–800) samples will be discussed below.

We also investigated the decay behavior of photoexcited carriers in these $ZnIn_2S_4$ samples by time-resolved photoluminescence emission decay spectra. Fig. 7 shows the emission decay traces of the $ZnIn_2S_4$-T (T=400–800) samples at room temperature. These emission traces were analyzed using biexponential decay kinetics, which were found to be satisfactory in the determination of emission lifetimes. The kinetic parameters for these $ZnIn_2S_4$ samples are summarized in Table 1. A biexponential kinetic analysis was carried out using the expression (1), and the average lifetime $\langle\tau\rangle$ was determined using the Eq. (2):

$$y = a_1 e^{-(t/\tau_1)} + a_2 e^{-(t/\tau_2)}, \quad (1)$$

$$\langle\tau\rangle = \frac{a_1\tau_1^2 + a_2\tau_2^2}{a_1\tau_1 + a_2\tau_2}, \quad (2)$$

where y is the impulse function decay at time t, and has an associated time constant, τ_i (i=1, 2), and amplitude, a_i (i=1, 2).

Obviously, in contrast to the fast decay curves of the $ZnIn_2S_4$-400 sample with cubic structure, the decay kinetics of the $ZnIn_2S_4$-T (T=500–800) samples were slower. In detail, the decay lifetime of carriers in cubic $ZnIn_2S_4$ ($ZnIn_2S_4$-400) was ca. 2.96 μs, while the decay lifetime of carriers was prolonged with crystal structure gradually changing from cubic to rhombohedral and the longest decay lifetime of carriers was observed in $ZnIn_2S_4$-700 to be ca. 6.91 μs. However, the decay lifetime of carriers in rhombohedral $ZnIn_2S_4$ ($ZnIn_2S_4$-800) was shortened to 4.83 μs. That is to say, the decay lifetime of carriers in the $ZnIn_2S_4$ samples with mixed phases of cubic and rhombohedral was prolonged compared to the $ZnIn_2S_4$ sample with counterpart cubic or rhombohedral single phase. Such prolongation of decay lifetime should be due to the co-existence of cubic and rhombohedral phases in the $ZnIn_2S_4$-T (T=500–800) samples, as indicated by the fact that the recombination of electron and hole pairs could be retarded by the enhanced charge separation between two phases [46].

3.4. Photocatalytic activity

Fig. 8 shows the photocatalytic activity for H_2 evolution from an aqueous Na_2SO_3/Na_2S solution over $ZnIn_2S_4$-T (T=400–800) under visible-light irradiation ($\lambda > 430$ nm). It can be seen from Fig. 8(A) that the H_2 production activities for these photocatalysts depended on their corresponding crystal structures closely.

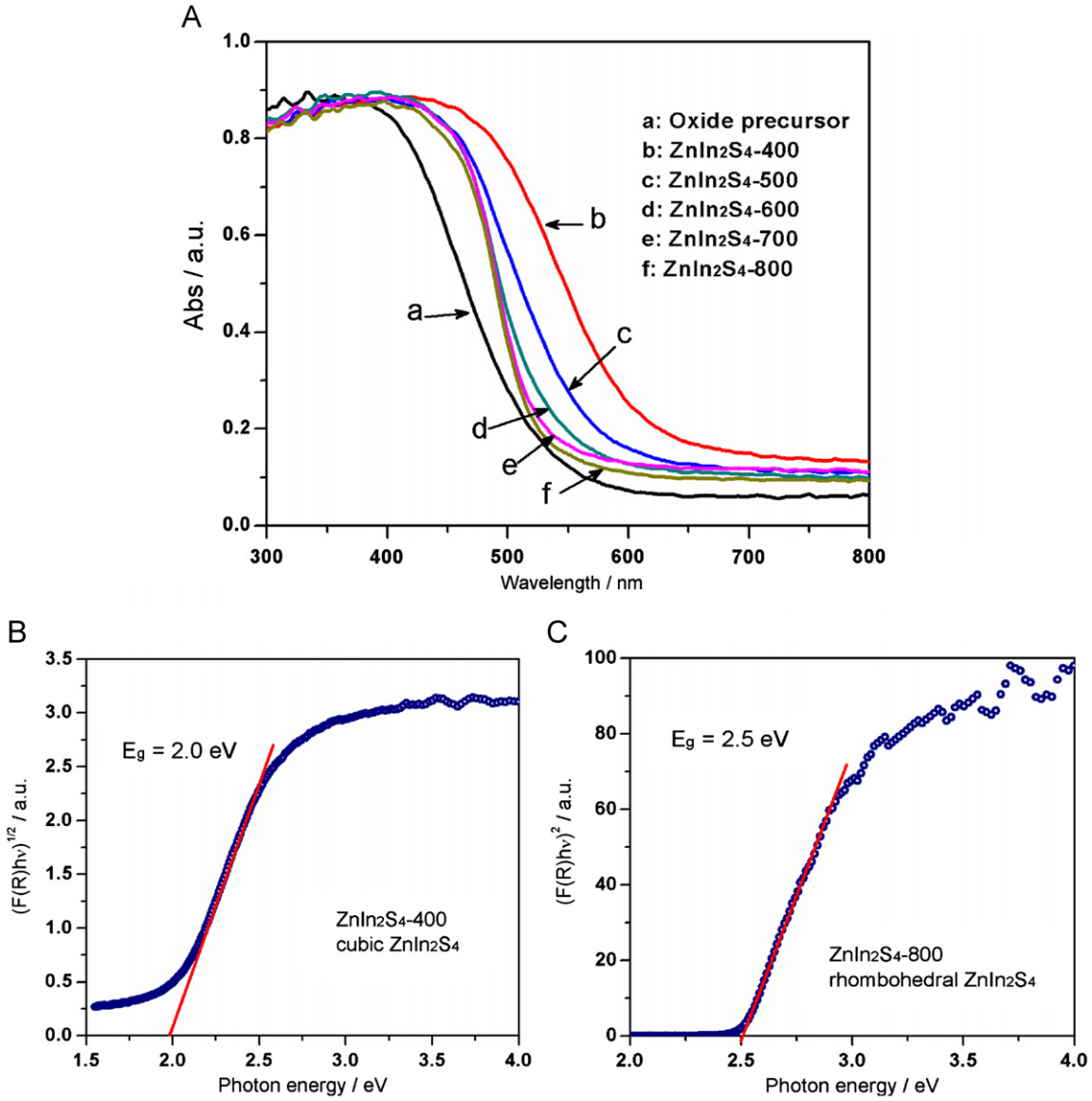

Fig. 5. (A) UV–vis absorption spectra of $ZnIn_2S_4$ synthesized in H_2S atmosphere at different temperatures, (a) oxide precursor, (b) 400 °C, (c) 500 °C, (d) 600 °C, (e) 700 °C and (f) 800 °C; (B) The calculated function $(F(R)h\nu)^{1/2}$ vs. photon energy plot for the $ZnIn_2S_4$-400 sample; and (C) The calculated function $(F(R)h\nu)^2$ vs. photon energy plot for the $ZnIn_2S_4$-800 sample.

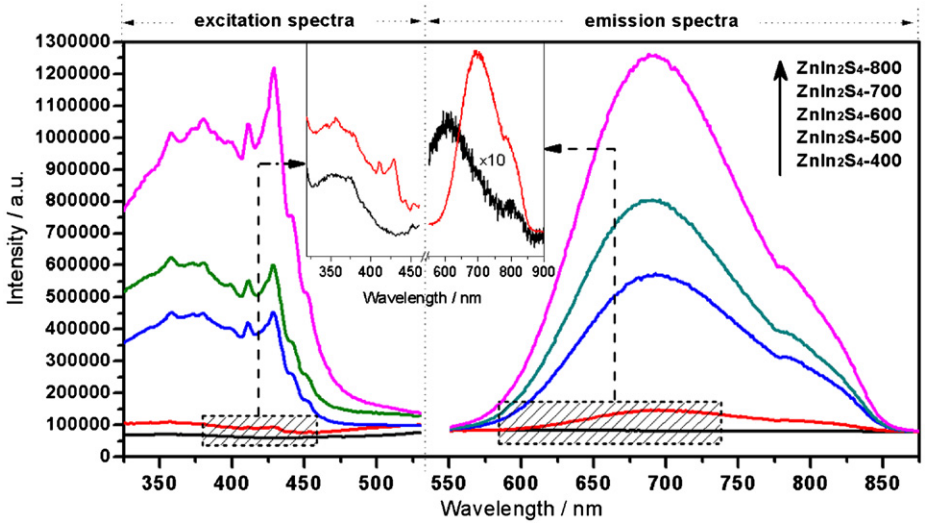

Fig. 6. Photoluminescence spectra of $ZnIn_2S_4$-T (T=400, 500, 600, 700, and 800) at room temperature. Excitation spectra: $ZnIn_2S_4$-400, monitored at 600 nm; $ZnIn_2S_4$-T (T=500–800), monitored at 690 nm. Emission spectra: $ZnIn_2S_4$-T (T=400–800), excited at 337 nm.

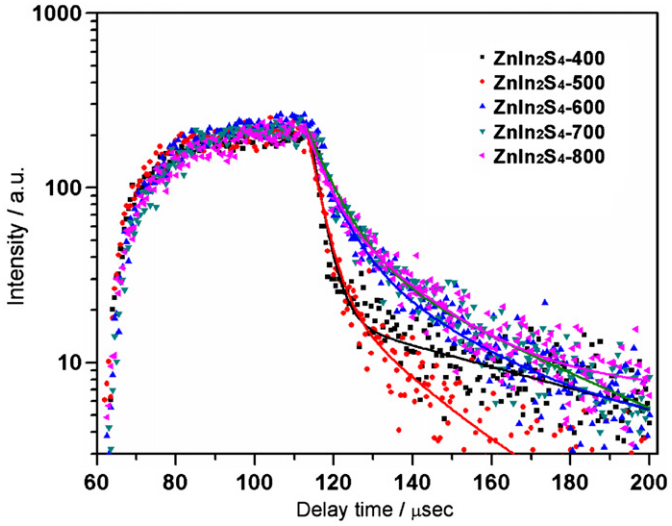

Fig. 7. Emission decay of $ZnIn_2S_4$-T (T=400, 500, 600, 700, and 800) at room temperature. $ZnIn_2S_4$-400, emission at 600 nm; $ZnIn_2S_4$-T (T=500–800), emission at 690 nm. The excitation wavelength was 337 nm. Solid lines represent the kinetic fit using biexponential decay analysis.

Table 1
Kinetic parameters of the $ZnIn_2S_4$ emission decay analysis.

$ZnIn_2S_4$ sample	Emission (nm)	a_1	τ_1 (μs)	a_2	τ_2 (μs)	$\langle\tau\rangle$ (μs)	$\chi 2$
$ZnIn_2S_4$-400	600	4.435E+011	2.96	44.29	71.22	2.96	1.886
$ZnIn_2S_4$-500	690	3.091E+010	3.34	520.4	21.15	3.34	0.944
$ZnIn_2S_4$-600	690	3.201E+009	3.79	1307	21.65	3.79	1.058
$ZnIn_2S_4$-700	690	1.686E+006	6.89	219.3	39.27	6.91	1.107
$ZnIn_2S_4$-800	690	6.216E+007	4.82	1732	20.20	4.83	1.149

The $ZnIn_2S_4$-400 sample with cubic structure almost displayed no activity for photocatalytic H_2 evolution; while the photocatalytic activity was markedly enhanced with the appearance of rhombohedral phase in the $ZnIn_2S_4$-500 sample. In previous studies [4,30], the cubic $ZnIn_2S_4$ was reported to show quite good photocatalytic activities for H_2 production, which is quite different from our results. Such discrepancy in photocatalytic activity may be due to the different synthetic methods, and the reason for the poor activity of cubic $ZnIn_2S_4$ in the present study will be discussed in the following section. With the crystal structure further changing to rhombohedral, the photocatalytic activity increased gradually and the highest activity was obtained over the $ZnIn_2S_4$-800 sample of pure rhombohedral phase. Moreover, as shown Fig. 8(B), the $ZnIn_2S_4$-800 sample presented to be more photocatalytically stable for H_2 evolution than the $ZnIn_2S_4$-700 sample, even though they displayed almost the same activity during the 20-h reaction period (shown in Fig. 8(A)). The relationship between crystal structure and photocatalytic activity will be discussed in detail as follows.

It is generally accepted that the larger the number of absorbed photons, the higher is the photocatalytic activity of a photocatalyst. As indicated by the absorption spectra in Fig. 5, the amount of absorbed photons should become smaller with crystal structure of $ZnIn_2S_4$ gradually changing from cubic to rhombohedral, because of the enlarged band gap. Then, $ZnIn_2S_4$ of pure rhombohedral phase ($ZnIn_2S_4$-800) with the largest band gap among these $ZnIn_2S_4$-T (T=400–800) samples should exhibit the lowest H_2 evolution rate. Contrary to this deduction, $ZnIn_2S_4$-800 displayed the highest photocatalytic H_2 evolution rate among these $ZnIn_2S_4$-T (T=400–800) samples as visible-light-driven photocatalysts. Therefore, the

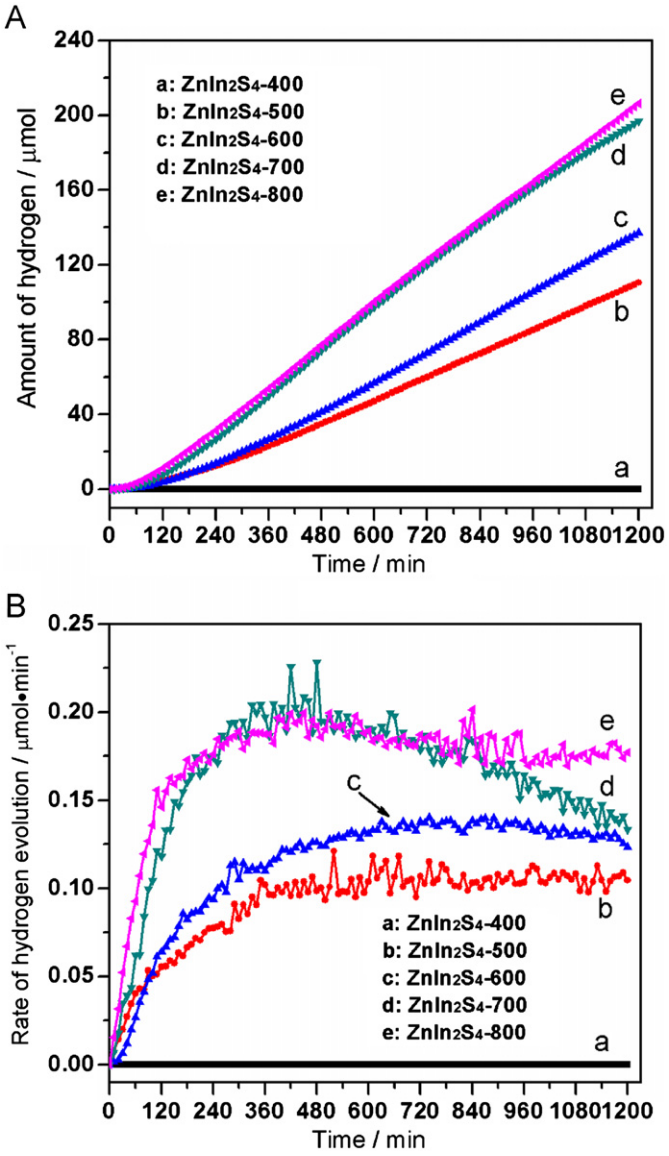

Fig. 8. Photocatalytic activity for H_2 evolution over Pt (1.0 wt%)-loaded $ZnIn_2S_4$-T (T=400, 500, 600, 700, and 800) from an aqueous Na_2S/Na_2SO_3 solution under visible light irradiation ($\lambda > 430$ nm).

difference in photocatalytic activity of $ZnIn_2S_4$-T (T=400–800) should be controlled by some other factors rather than band gap.

It was reported that, if non-radiative transition dominates in a photocatalyst, the number of electrons and holes to be involved in the photocatalytic reaction is decreased, thus resulting in a decrease in the photocatalytic activity [45,47]. As shown in Fig. 6, the domination of non-radiative transition indicated by the severe photoluminescence quenching was observed on $ZnIn_2S_4$-400 of pure cubic phase, and hence this should correspond to the poor photocatalytic activity of this cubic $ZnIn_2S_4$. For the $ZnIn_2S_4$-T (T=500–700) samples with crystal structure gradually changing from cubic to rhombohedral, the efficiency of non-radiative transition turned to be lower along with emission intensity increasing, which indicated that the number of electrons and holes involved in the photocatalytic reaction increased gradually. Therefore, the photocatalytic activity for H_2 evolution over the $ZnIn_2S_4$-T (T=400–700) samples presented to be a increasing trend with the change of crystal structure from cubic to rhombohedral, as shown in Fig. 8. The decay behavior of photogenerated carriers is the other key factor affecting the photocatalytic activity. As shown in Fig. 7 and Table 1,

the decay lifetime of carriers in the $ZnIn_2S_4$-T (T=400–700) samples is gradually prolonged from 2.96 to 6.91 μs. This indicated that the recombination probability of electron and hole pairs was retarded, which resulted in the increasing photocatalytic performances from $ZnIn_2S_4$-400 to $ZnIn_2S_4$-700. By further comparison, one could only observe slightly better photocatalytic performance for H_2 evolution over $ZnIn_2S_4$-800 than $ZnIn_2S_4$-700, even though $ZnIn_2S_4$-800 possessed much more photoinduced charges potentially available for photocatalysis as evidenced by its much higher emission intensity in Fig. 6. However, while considering the lifetime of photoinduced charges, it is possible to give a reasonable explanation on the similar activity between $ZnIn_2S_4$-800 and $ZnIn_2S_4$-700, as shorter lifetime of charges in $ZnIn_2S_4$-800 (4.83 vs. 6.91 μs in $ZnIn_2S_4$-700) meant the faster charge recombination, which was disadvantageous for photocatalytic H_2 evolution. By the way, the better photocatalytic stability of $ZnIn_2S_4$-800 as shown in Fig. 8(B) should be due to its better crystallinity of rhombohedral phase than that of $ZnIn_2S_4$-700 as indicated by XRD analysis.

4. Conclusion

In summary, a series of $ZnIn_2S_4$ was synthesized via a thermal sulfidation method at different temperatures. With sulfidation temperature rising from 400 to 800 °C, the crystal structure of $ZnIn_2S_4$ gradually changed from cubic to rhombohedral, along with the increasing photocatalytic activity for H_2 evolution under visible light irradiation from an aqueous solution containing Na_2S/Na_2SO_3 as sacrificial reagents. This difference in photocatalytic activity should be related with the number and the lifetime of photogenerated charges useable for photocatalytic reaction, which was proved to be induced by different crystal structures of these $ZnIn_2S_4$ samples. Photoluminescence properties revealed the different dynamics of photogenerated carriers, which played an important role in the photocatalytic performances of $ZnIn_2S_4$ with different crystal structures. This study provided some in-depth understanding on phase change and related effects on optical properties and photocatalytic performances. It is to be wished that these information would be useful for further development of such kind of photocatalyst.

Acknowledgments

The authors gratefully acknowledge the financial supports of the National Natural Science Foundation of China (Nos. 50821064 and 91010012) and National Basic Research Program of China (No. 2009CB220000). One of the authors (S.S.) was supported by "the Fundamental Research Funds for the Central University".

References

[1] A. Fujishima, K. Honda, Nature 238 (1972) 37–38.
[2] X. Chen, S. Shen, L. Guo, S.S. Mao, Chem. Rev. 110 (2010) 6503–6570.
[3] H. Yan, J. Yang, G. Ma, G. Wu, X. Zong, Z. Lei, J. Shi, C. Li, J. Catal. 266 (2009) 165–168.
[4] Z. Lei, W. You, M. Liu, G. Zhou, T. Takata, M. Hara, K. Domen, C. Li, Chem. Commun. 17 (2003) 2142–2143.
[5] S. Shen, L. Zhao, L. Guo, J. Phys. Chem. Solids 69 (2008) 2426–2432.
[6] S. Shen, L. Zhao, Z. Zhou, L. Guo, J. Phys. Chem. C 112 (2008) 16148–16155.
[7] K. Kobayakawa, A. Teranishi, T. Tsurumaki, Y. Sato, A. Fujishima, Electrochim. Acta 37 (1992) 465–467.
[8] L. Zheng, Y. Xu, Y. Song, C. Wu, M. Zhang, Y. Xie, Inorg. Chem. 48 (2009) 4003–4009.
[9] W.J. Fan, Z.F. Zhou, W.B. Xu, Z.F. Shi, F.M. Ren, H.H. Ma, S.W. Huang, Int. J. Hydrogen Energy 35 (2010) 6525–6530.
[10] S. Shen, L. Zhao, L. Guo, Int. J. Hydrogen Energy 35 (2010) 10148–10154.
[11] J.S. Jang, S.H. Choi, N. Shin, C. Yu, J.S. Lee, J. Solid State Chem. 180 (2007) 1110–1118.
[12] J.S. Jang, P.H. Borse, J.S. Lee, S.H. Choi, H.G. Kim, J. Chem. Phys. 128 (2008) 154717.
[13] M. Tabata, K. Maeda, T. Ishihara, T. Minegishi, T. Takata, K. Domen, J. Phys. Chem. C 114 (2010) 11215–11220.
[14] H. Kaga, K. Saito, A. Kudo, Chem. Commun. 46 (2010) 3779–3781.
[15] I. Tsuji, Y. Shimodaira, H. Kato, H. Kobayashi, A. Kudo, Chem. Mater. 22 (2010) 1402–1409.
[16] Z. Zhang, J. Zhang, T. Wu, X. Bu, P. Feng, J. Am. Chem. Soc. 130 (2008) 15238–15239.
[17] N. Zheng, X. Bu, H. Vu, P. Feng, Angew. Chem. 117 (2005) 5433–5437.
[18] A. Kudo, A. Nagane, I. Tsuji, H. Kato, Chem. Lett. 31 (2002) 882–883.
[19] I. Tsuji, H. Kato, H. Kobayashi, A. Kudo, J. Am. Chem. Soc. 126 (2004) 13406–13413.
[20] I. Tsuji, H. Kato, H. Kobayashi, A. Kudo, J. Phys. Chem. B 109 (2005) 7323–7329.
[21] T. Torimoto, T. Adachi, K. Okazaki, M. Sakuraoka, T. Shibayama, B. Ohtani, A. Kudo, S. Kuwabata, J. Am. Chem. Soc. 129 (2007) 12388–12389.
[22] I. Tsuji, H. Kato, A. Kudo, Angew. Chem. Int. Ed. 44 (2005) 3565–3568.
[23] I. Tsuji, H. Kato, H. Kobayashi, A. Kudo, Chem. Mater. 18 (2006) 1969–1975.
[24] Y. Li, G. Chen, C. Zhou, J. Sun, Chem. Commun. 15 (2009) 2020–2022.
[25] Y. Li, G. Chen, Q. Wang, X. Wang, A. Zhou, Z. Shen, Adv. Funct. Mater. 22 (2010) 3390–3398.
[26] S. Shen, L. Zhao, L. Guo, Int. J. Hydrogen Energy 33 (2008) 4501–4510.
[27] S. Shen, L. Zhao, L. Guo, Mater. Res. Bull. 44 (2009) 100–105.
[28] M. Li, J. Su, L. Guo, Int. J. Hydrogen Energy 33 (2008) 2891–2896.
[29] X. Gou, F. Cheng, Y. Shi, L. Zhang, S. Peng, J. Chen, P. Shen, J. Am. Chem. Soc. 128 (2006) 7222–7229.
[30] B. Chai, T. Peng, P. Zeng, X. Zhang, X. Liu, J. Phys. Chem. C 115 (2011) 6149–6155.
[31] K.J. Range, W. Becker, A.Z. Weiss, Naturforsch 24B (1969) 811–812.
[32] Y. Chen, S. Hu, W. Liu, X. Chen, L. Wu, X. Wang, P. Liu, Z. Li, Dalton Trans. 40 (2011) 2607–2613.
[33] D. Jing, L. Guo, J. Phys. Chem. B 110 (2006) 11139–11145.
[34] K. Zhang, D. Jing, C. Xing, L. Guo, Int. J. Hydrogen Energy 32 (2007) 4685–4691.
[35] S.A. López-Rlvera, L. Martínez, B. Fontal, W. Giriat, F. Medina, Semicond. Sci. Technol. 10 (1995) 645–652.
[36] W.K. Unger, H. Meuth, J.C. Irwin, H. Pink, Phys. Statua Solidi (a) 46 (1978) 81–87.
[37] G. Baldini, R.L. Aggarwal, B. Lax, S.H. Shin, J.C. Tsang, Lett. Nuovo Cim. 5 (1972) 1062–1066.
[38] A. Kudo, M. Sekizawa, Catal. Lett. 58 (1999) 241–243.
[39] A. Kudo, M. Sekizawa, Chem. Commun. 15 (2000) 1371–1372.
[40] G. Liu, L. Zhao, L. Ma, L. Guo, Catal. Commun. 9 (2008) 126–130.
[41] S. Shionya, Y. Tamoto, J. Phys. Soc. Jpn. 19 (1964) 1142–1149.
[42] J.K. Mishra, S. Bhunia, S. Banerjee, P. Banerji, J. Lumin. 128 (2008) 1169–1174.
[43] H. Zeng, G. Duan, Y. Li, S. Yang, X. Xu, W. Cai, Adv. Funct. Mater. 20 (2010) 561–572.
[44] V.F. Zhitar, V.Y. Raylyan, S.I. Radautsan, Il Nuovo Cim. 2 (1983) 1919–1922.
[45] H. Kato, A. Kudo, J. Photochem. Photobiol. A: Chem. 145 (2001) 129–133.
[46] J. Zhang, Q. Xu, Z. Feng, M. Li, C. Li, Angew. Chem. Int. Ed. 47 (2008) 1766–1769.
[47] Y. Yuan, Z. Zhao, J. Zheng, M. Yang, L. Qiu, Z. Li, Z. Zou, J. Mater. Chem. 20 (2010) 6772–6779.